Solid and grid sphere current collection in view of the tethered satellite system TSS 1 and TSS 1R mission results

G. V. Khazanov, E. Krivorutsky, and R. B. Sheldon

National Space Science and Technology Center, NASA Marshall Space Flight Center, Huntsville, Alabama, USA

Received 23 February 2005; revised 1 August 2005; accepted 14 September 2005; published 13 December 2005.

[1] Passive end body plasma contactors have been operationally validated in space and have been shown to provide a simple, effective, and robust means of current collection at the positive terminal of an electrodynamic tether system. A grid sphere has been suggested as a possible end body since it potentially has distinct advantages compared to a solid sphere, including a lower neutral dynamic drag and a higher current-to-mass ratio. This paper estimates the maximum current collected by a grid sphere, taking into account its orbital motion and ion production inside the grid sphere. We first review the data from the tethered satellite system (TSS 1) and the TSS 1R flights, formulate a model for current collection by a solid sphere, and suggest how to incorporate it into the grid sphere current collection estimate. Then we calculate the potential distribution inside the grid sphere and the potential distribution outside the solid sphere for the same system parameters. Finally, we estimate the maximum current collected by a grid sphere depending on its transparency.

Citation: Khazanov, G. V., E. Krivorutsky, and R. B. Sheldon (2005), Solid and grid sphere current collection in view of the tethered satellite system TSS 1 and TSS 1R mission results, *J. Geophys. Res.*, *110*, A12304, doi:10.1029/2005JA011100.

1. Introduction

[2] There are a number of space applications for electrodynamic tether systems that require high current on the order of dozens of amperes for operation. Closure of the electric circuit of an electrodynamic tether necessarily requires an electrical connection between the tether's positive electrode and the ambient ionospheric plasma, where the anode may take various forms. It may be a spherical solid surface conducting end body that has been systematically studied for the TSS missions, or it may be the positively biased portion of the tether itself as was planned for the ProSEDS flight demonstration. No matter what the geometry of the collection area might be, the collection, for example, of 10 A requires a large current collection surface on the order of 1000 m^2, because ionospheric thermal current density is only about 10 mA/m^2. That is why there is a constant search for the most efficient and light end body contactor.

[3] Passive end body contactors have been validated in space and provide a simple, effective, and robust means of current collection at the positive terminal of an electrodynamic tether system. Determination of the most effective type of contactor is primarily based on its current collection efficiency, dynamic drag, and mass. *Stone and Gierow* [2001], *Stone et al.* [2002] have proposed a grid sphere end body with high transparency, about 90%. They argue that such a design has distinct advantages, providing a large current collection area, low dynamic drag and high current-to-mass ratio. Their preliminary results regarding the grid sphere performance, based on a calculation of the current collection for cylindrical and spherical bodies, suggest that it may be a simple and reliable means of developing large tether currents, unencumbered by high power requirements, hot filaments, expendables, and the complex electronics associated with existing active contactor devices.

[4] Their analysis of current collection for a grid sphere assumed that there is no positive charge inside the sphere and neglected the tether system orbital motion. The motion, as known from the results of the TSS 1 and TSS 1R missions, substantially increases the current collected by a solid sphere [*Wright et al.*, 1996; *Thompson et al.*, 1998]. We present below a calculation of the maximum current collection by a grid sphere taking into account the orbital motion, as well as the ion production from ionization of neutrals by incoming energetic electrons inside the grid sphere. The paper is organized as follows: Section 2 reviews the current collection of TSS 1 and the TSS 1R flights, and presents a model for solid sphere current collection; section 3 describes the potential distribution formation inside the grid sphere; section 4 suggests how to incorporate the results of sections 2 and 3 into the grid sphere current collection studies and calculate the upper bound for this current; and section 5 summarizes the results.

2. Model for a Solid Sphere Current Collection

[5] One of the major goals of the TSS 1 and TSS 1R flights was to study the electron current collected by a solid

0148-0227/05/2005JA011100$09.00

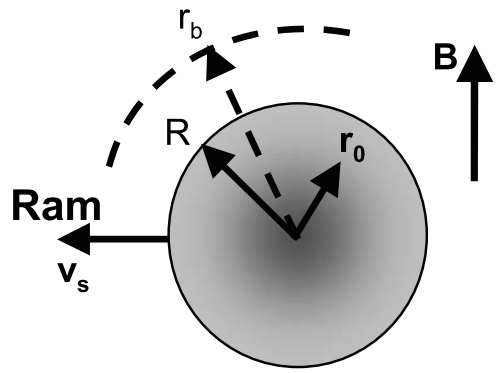

Figure 1. Schematic of the model. The satellite moves from right to left with velocity $\vec{v}_s$; $\vec{B}$ is the ambient magnetic field; the sphere (grid sphere) radius is R; the shaded area is the region close to neutral; $\vec{r}_0$ is an arbitrary point where an ion is produced; and r_b indicates the boundary between the regions of one- and two-dimensional electron acceleration. The tether is along the normal to the plane.

sphere subsatellite at a large positive voltage with respect to the surrounding plasma. During both flights, the subsatellite's current collection was observed to be in excess of the values predicted by *Parker and Murphy* [1967] by a rough factor between 2 and 6, when the potential was between 20–1000 V positive with respect to the subsatellite's surroundings. Such an outcome was very surprising in view of the large mean electron thermal speed (212 km/s for the thermal energy ~0.1 eV), compared with their relative drift speed about 8 km/s due to the satellite's orbital motion. To explain these results, several theoretical approaches have been developed [*Dobrowolny et al.*, 1995; *Vannaroni et al.*, 1998; *Katz et al.*, 1994; *Laframboise*, 1997; *Cooke and Katz*, 1998; *Ma and Schunk*, 1998; *Singh and Leung*, 1998] that focused mainly on the TSS 1 or TSS 1R observations. In this section we present a model for solid sphere current collection based on these theoretical results and the experimental data from both TSS missions. Using this model, we will estimate the maximum current collected by a grid sphere.

[6] For a solid sphere contactor we assume that the region outside the sphere can be divided in two shells (Figure 1). The inner region, starting from the sphere surface, is assumed to be spherically symmetric with a Boltzmann ion distribution and one-dimensionally accelerated electrons [*Laframboise and Parker*, 1973; *Laframboise*, 1997]. The outer boundary of this region, r_b, is the isopotential surface that reflects the ion flux related to satellite motion [*Laframboise*, 1997; *Cooke and Katz*, 1998] and collects a current equal to the upper limit current found by *Laframboise and Parker* [1973] for two-dimensional electron acceleration. According to *Laframboise and Parker* [1973], this current, collected in our model at the boundary of the first region, is

$$\frac{I}{I_0} = \frac{1}{\sqrt{\pi}}\frac{r_b^2}{R^2}\left(\sqrt{\chi_b} + \frac{1}{2\sqrt{\chi_b}}\right), \qquad (1)$$

where R is the sphere radius, r_b is the boundary radius, and $\chi_b = e\varphi_b/kT$ is the normalized potential (φ_b is the potential of the boundary, e is the elementary charge, T is the plasma temperature, and k is the Boltzmann constant). The current is normalized to $I_0 = \pi R^2 e n_\infty \sqrt{8kT/\pi m}$, the random electron current. Here n_∞ is the undisturbed plasma density and it is assumed in expression (1) that the current is collected only by the leading ram hemisphere. Following *Cooke and Katz* [1998] and *Laframboise* [1997], the potential at the boundary is set equal to the energy needed to reflect the ions, defined by the normal component of the ion velocity relative to the satellite and averaged over the sphere surface. So $\chi_b = E_i/3kT$ where $E_i \approx 5$ eV is the ion kinetic energy.

[7] To calculate the current from equation (1), the radius of the boundary, r_b, that separates the regions of one- and two-dimensional acceleration should be found. To calculate r_b, the Poisson equation in the region between the grid sphere surface and the boundary has been solved:

$$\frac{1}{x^2}\frac{d}{dx}x^2\frac{d\chi}{dx} = \frac{R^2}{\lambda_D^2}\left(\frac{2}{\sqrt{\pi\chi}} - e^{-\chi}\right), 1 \le x = \frac{r}{R} \le \frac{r_b}{R}, \chi = \frac{e\varphi}{kT}. \quad (2)$$

The electron density here corresponds to the one-dimensional acceleration case [*Laframboise and Parker*, 1973] with $\chi \gg 1$, where λ_D is the Debye length. At the outer boundary of this region, r_b, the electron density is chosen equal to the ion density, which because of ion reflection is set at twice the undisturbed ion density [*Laframboise*, 1997].

[8] To calculate the unknown radius r_b from equation (2), a third condition is needed, which could be provided by the solution in the outer domain $r > r_b$. Instead, we simplify the problem by assuming that the boundary r_b between the regions of one- and two-dimensional acceleration can be identified as the position where the electric field abruptly drops and changes sign, indicating that further out the one-dimensional electron density distribution is not valid. As can be expected from equation (2), it is also the radius where the potential, χ, is close to zero. Such approach is partly justified by the results of the numerical simulations [*Ma and Schunk*, 1998; *Singh and Leung*, 1998], where

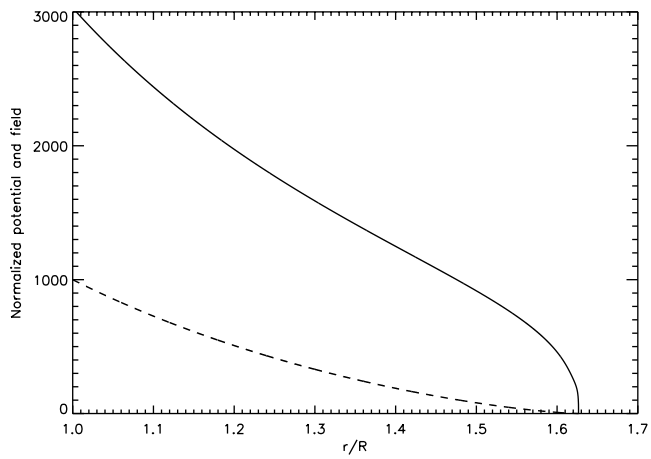

Figure 2. Normalized potential distribution $\chi = e\varphi(x)/kT$ (dashed line) and electric field $-d\chi/dx$ (solid line) in the region of one-dimensional electron acceleration $x = r/R$.

Table 1. Normalized Currents Collected by TSS-1 and TSS-1R Missions I/I_0, Calculated Currents I_c/I_0, and Their Ratio I/I_c

n_∞ 10^{-10}, m^{-3}	T, °K	φ_R, V	I/I_0	r_b/R	I_c/I_0	I/I_c
2.5	1160	44.5	7.0	1.82	7.7	0.91
70	1200	30	2.9	1.15	3.0	0.97
8.4	1600	235	10.6	2.22	9.9	1.07
32	1650	850	13.3	2.5	12.4	1.07

two regions with different potential structure are observed, as well as by the agreement of our results presented below with experimental data.

[9] So the boundary radius, r_b, has been defined as the radius where simultaneously the potential is close to zero and the electric field abruptly drops and changes sign. Equation (2) has been solved numerically by starting from the sphere surface with the known potential and some potential first derivative. The potential first derivative on this surface was adjusted until the radius defined above as the boundary has been found. Outside this boundary the assumed density distribution is no longer applicable. We plot the normalized potential and the first derivative of this potential over the normalized length, $x = r/R$, for $\chi_R = e\varphi_R/kT = 1000$ and $R/\lambda_D = 135$ in Figure 2. As can be seen from Figure 2, the transition region near the boundary is very narrow and the boundary radius r_b is easy to identify. The same holds true for all system parameters used in our calculations. To verify the model, such calculations have been performed on the set of system parameters for which experimental data are available. Table 1 compares the results of these calculations with the data from TSS 1 [*Dobrowolny et al.*, 1995] and TSS 1R [*Vannaroni et al.*, 1998] missions for very different system parameters. As can be seen, the ratio of observed to calculated currents, I/I_c, shows good agreement despite large variations in plasma density, temperature and sphere potential.

[10] Figures 3 and 4 plot the results of these calculations along with all the data from *Dobrowolny et al.* [1995] and *Vannaroni et al.* [1998]. Our Figure 3 reproduces Figure 2 from the first paper (TSS 1 mission) with the results of our calculations inserted as the red dots. The sphere potential and plasma parameters for these calculations, presented in Table 2, are taken from their Table 1. The measured temperature is 0.1 eV. The three curves in Figure 3 correspond to three models of current collection: the Parker-Murphy model (P-M 1), the Alpert model [*Alpert et al.*, 1965] and the Parker-Murphy model modified for sweeping effects of the velocity flow (P-M 2). Figure 4 reproduces Figure 1 from the paper of *Vannaroni et al.* [1998] (TSS 1R mission). They compared their observed currents with that predicted by the Parker-Murphy and Alpert models. Again, our results are added as red dots. As can be seen from Figures 3 and 4, the results of our calculations are in reasonable agreement with the measurements except for a few low-voltage cases presented in Figure 4a, where the measured current-voltage characteristic is quite different from all other measurements. Our model predicts a current close to that of the Alpert model, which describes the current collection in an unmagnetized plasma. It should be noted that the results from the Alpert model shown in Figures 3 and 4 are obtained under the condition $e\varphi_R/kT \geq (R/\lambda_D)^{4/3}$ [*Dobrowolny et al.*, 1995; *Vannaroni et al.*, 1998; *Alpert et al.*, 1965], which is not satisfied for typical plasma parameters at altitudes about 300–400 km for large sphere radii. For the system parameters of Figure 4a, $(e\varphi_R/kT)(R/\lambda_D)^{-4/3} \leq 0.24$. According to the Alpert model, if this parameter is much less than one, the current should be constant, $I/I_0 = 1.5$, so, the Alpert model is not applicable. For an electrodynamic tether drawing even fewer amperes, the radius must be so large as to make this parameter much smaller than 1, also rendering the Alpert model inapplicable. This is the situation that exists in the case of a grid sphere that should have a large enough radius to collect a suitable current.

[11] The current collected by the solid sphere contactor (equation (1)) can be estimated for different system parameters with the help of Table 3, which tabulates the magnitude of the normalized boundary radii, r_b/R, for the set of two dimensionless parameters, R^2/λ_D^2 and $e\varphi_R/kT$ determining the solution of equation (2). As can be seen from Table 3 the boundary radius is inversely proportional to R^2/λ_D^2 which can be approximated as $(r_b/R)^2 \propto (\lambda_D^2/R^2)^\sigma$ with an accuracy of about 20%. The exponent σ depends on the normalized potential of the sphere surface, for example, $\sigma = 0.12, 0.23, 0.28$ for $e\varphi_R/kT = 10^3$, 5×10^3, 10^4 respectively.

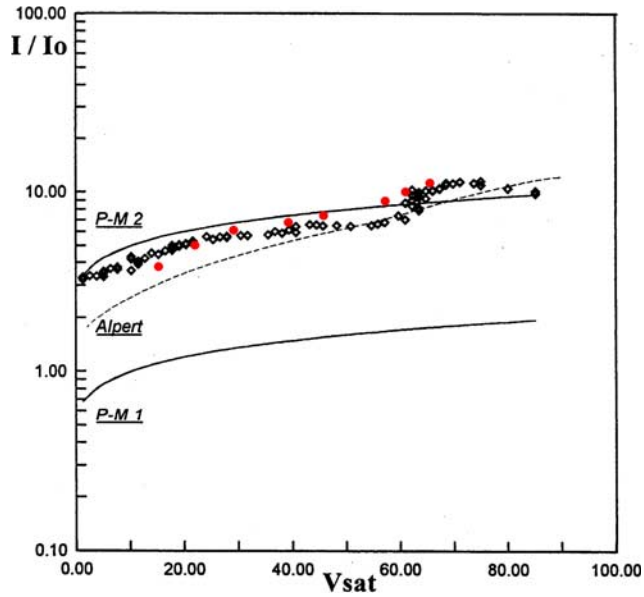

Figure 3. Comparison between experimental data (diamonds) and theoretical models. The satellite potential is represented on the abscissas and the normalized current on the ordinates. Red dots plot the results of this paper. Adapted from *Dobrowolny et al.* [1995, Figure 2].

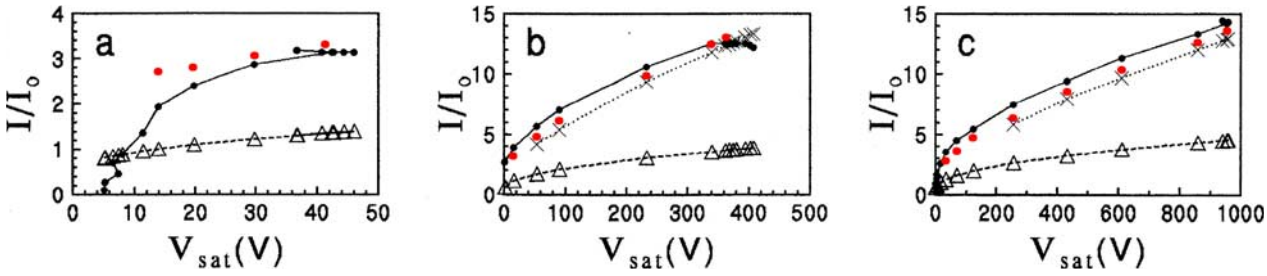

Figure 4. Comparison between the experimental I-V characteristic (dots) and theoretical models (crosses for the Alpert model and triangles for the Parker-Murphy model): (a) first IV-24 with experimental conditions Φ_{emf} = 1200 V, $n_e = 7.0 \times 10^{11}$ m^{-3}, and T_e = 1200 K; (b) second IV-24 with Φ_{emf} = 1075 V, $n_e = 8.4 \times 10^{10}$ m^{-3}, and T_e = 1600 K; (c) third IV-24 with Φ_{emf} = 3463 V, $n_e = 3.2 \times 10^{11}$ m^{-3}, and T_e = 1650 K). Red dots plot the results from this paper. Adapted from *Vannaroni et al.* [1998, Figure 1].

[12] We use this model to estimate the upper bound of the current collected by the grid sphere.

3. Potential Interior of the Grid Sphere

[13] Following *Stone et al.* [2002], we assume that a grid sphere is characterized by the transparency α, equal approximately to the ratio of the part of the sphere surface without mesh to its total surface. Electrons accelerated by the grid sphere potential penetrate inside the grid sphere and cause impact ionization of neutrals. The secondary electrons produced by this process will be expelled quickly from the grid sphere, but the ions will be kept inside it by the charge of the high-energy incoming electrons. The grid sphere ion content depends on the rate of ion production, recombination, and their flux through the grid sphere surface. For an ionospheric altitude about 300 km and above, recombination is slow compared to the ionization rate and can be neglected, as can be seen from a following simple estimate.

[14] The main neutral components at this altitude are molecular nitrogen, and atomic oxygen. We can assume that the ionization cross section due to collisions with the energetic electrons for all of these components is of the same order of magnitude. The ions of atomic oxygen have the longest lifetime at this altitude, which is determined by ion-molecular reactions of O^+ with nitrogen neutral molecules [*Schunk and Nagy*, 2000]. This lifetime is $t_{lt} \sim 1000$ s. Other ions, produced by collisions with fast electrons, are neutralized on a shorter timescale; so their contribution is about five times smaller and will be neglected. The number of oxygen ions produced per unit volume per second by ionization is $\sigma N_O j$, where σ is the cross section for impact ionization, N_O is the atomic oxygen density, and j is the electron flux density. In quasi-static equilibrium, the ionization and recombination processes balance, which can be written as $\sigma N_O j = n_i/t_{lt}$, where n_i is the oxygen ion density. For $\sigma = 10^{-20}$ m^2, $N_o = 5 \times 10^{14}$ m^{-3}, and thermal electron flux $j = n_\infty \sqrt{kT/2\pi m}$, this leads to an oxygen ion density more than two orders of magnitude larger than the density of the undisturbed plasma, n_∞, for particle energies $kT \sim 0.1$ eV, as can be seen from their ratio $n_i/n_\infty = t_{lt}\sigma N_o \sqrt{kT/2\pi m}$. Therefore the role of recombination is negligible, and the ion content of the grid sphere is determined by the balance between oxygen ion production and their flux through the grid sphere surface.

[15] In contrast to the ions, the density of the locally produced secondary electrons will be much smaller than the density of penetrating electrons. The secondary electron production rate inside the grid sphere is roughly equal to the grid sphere volume multiplied by the electron density production rate, which is approximately the same as for ions, $\sigma N_O j$. The flux of the secondary electrons through the grid sphere surface is $4\pi R^2 j_s$, where the grid sphere radius is R, and j_s is the secondary electron flux density. In equilibrium the production and losses should be equal, $R\sigma N_O j \sim j_s$. Since the energy of the incoming electrons is defined by the grid sphere surface potential, φ_R, this equilibrium becomes $R\sigma N_O \sqrt{e\varphi_R/K_s} \sim n_s/n$, where K_s and n_s are the kinetic energy and density of a secondary electrons, and n is the density of incoming electrons. The energy ratio is $e\varphi_R/K_s \sim 20-50$ for impact ionization of the oxygen atoms, if the grid sphere surface potentials are in the range 100–1000 V. For the grid sphere radius $R \sim 10$ m, using σ and N_o from the previous estimate, n_s/n is less than 0.001 justifying our neglect of the secondary electrons in the calculations below.

[16] To calculate the potential distribution inside the grid sphere the electron and the ion densities are needed. The ionized neutrals have a large velocity relative to the grid sphere compared to their thermal velocity because of the grid sphere orbital motion. In the coordinate system that is attached to the grid sphere, ions are born with a velocity of about 8 km/s, giving them a transit time through the grid sphere of about 0.1–1 ms for grid sphere radii in the range of 1–10 m. Because of the large interior scale of the grid sphere compared to the Debye length, it can be expected that in equilibrium most plasma inside the grid sphere will

Table 2. Current, Voltage, and Electron Density Measured by the TSS 1 Mission [From *Dobrowolny et al.*, 1995, Table 1]

n_∞ 10^{-10}, m^{-3}	I, mA	φ_R, V
4.5	14.65	14.0
4.0	14.02	20.3
3.5	13.39	28.8
3.0	12.13	38.1
2.5	11.97	44.5
2.2	10.71	57.2
2.0	11.97	61.0
1.8	11.97	64.8

Table 3. Parameter r_b/R for the Solid Sphere Current (Equation 1)

	$R^2/\lambda_D{}^2 \times 10^{-5}$									
$e\varphi_R/kT$	0.18	0.73	2.9	5.1	6.5	11.6	18.1	46	81	127
1000	1.63	1.36	1.20	1.15	1.13	1.10	1.08	1.05	1.04	1.03
5000	2.54	1.93	1.54	1.43	1.38	1.30	1.25	1.16	1.12	1.10
10000	3.19	2.35	1.81	1.65	1.59	1.46	1.38	1.26	1.20	1.16

be quasi-neutral, at least for large sphere radii and dense plasma. Maintaining quasi-neutrality inside the grid sphere requires that the ions be quasi-trapped with a characteristic time that can be estimated assuming equal densities of ions and penetrating electrons. The time needed to produce an ion density $n_i \sim n_e$ with an ionization rate $\sigma N_O j$ is $t_{pr} \sim n_e/\sigma N_O j$, which is the characteristic time to replenish the ion population. With an electron velocity $v_e \propto \sqrt{\varphi_R}$ for high grid sphere surface potential, φ_R, this time can be rewritten as $t_{pr}[\text{sec}] \sim C/\sqrt{e\varphi_R/kT}$, where the constant C is about 1sec for the particle parameters used above. This is also the characteristic time that the ion should be kept inside the grid sphere to maintain plasma quasi-neutrality. Since this time is much longer than the transit time, even for high grid sphere potentials, the newborn ion must experience multiple reflections before leaving the grid sphere. Therefore a potential well inside the grid sphere must exist.

[17] The newborn ions can be described by a shifted Maxwell-Boltzmann distribution function describing particles in the presence of conservative force field,

$$f(t=0,\vec{r}_0,\vec{v}) = C_0 \exp\left(-\frac{e\varphi(\vec{r}_0)}{kT} - (\vec{v}-\vec{v}_s)^2\right). \quad (3)$$

Here $\vec{v}_s$ and $\vec{v}$ are the satellite and ion velocities normalized by $v_T = \sqrt{2kT/M}$, M is the mass of the oxygen ion, and $\varphi(\vec{r}_0)$ is the potential at the point where the ion is born (Figure 1). Because of multiple reflections inside the well the equilibrium distribution should be nearly isotropic in velocity space on a long timescale compared to the transit time. It means that the angle-dependent part of the distribution (3) vanishes for times longer than the transit time, which is also the time between ion "collisions" with the potential wall, leaving only the isotropic part. This isotropic part can be found as the angle-independent term of the function (3) when expanded in spherical harmonics in configuration and velocity space, or by averaging this function over all angles. Therefore the distribution function averaged over the oscillations in the well, which randomize the momentum but conserve the energy, will depend only on the distance from the center of the grid sphere, $r = |\vec{r}|$, and the ion speed $v = |\vec{v}|$. The angle-averaged part, f_0, of the initial distribution (3) is

$$f_0(t=0,r_0,v) = \frac{C_0}{2vv_s} e^{\left(-\chi(r_0)-\left(v^2+v_s^2\right)\right)} \sinh(2vv_s). \quad (4)$$

[18] The dependence of this distribution on r_0, v is independent of time so for times larger than the transition time, t_{tr}, the function is the same within a normalization constant, f_0 ($t > t_{tr}$, r_0, v) = cf_0 ($t = 0$, r_0, v).

[19] Equation (4) presents the velocity dependence of the ion distribution at the location r_0, where the particles are produced by ionization. At the location r the ion distribution can be found as the solution of the kinetic equation. Because the quasi-static distribution function is angle-independent in configuration as well as in velocity space, the kinetic equation reduces to $\mathrm{v}\dfrac{\partial \mathrm{f}}{\partial r} - \dfrac{e}{M}\dfrac{d\varphi}{dr}\dfrac{\partial f}{\partial \mathrm{v}} = 0$. The solution of this equation depends on the ions energy integral and can be obtained from equation (4) by setting $v \to \sqrt{v^2 + e[\varphi(r)-\varphi(r_0)]/kT}$, which can be checked by substituting directly into the kinetic equation.

[20] As previously mentioned, there are two length scales in the electrostatic problem of grid sphere interior potential calculation: the Debye length, and the size of the grid sphere. Because the grid sphere size is much larger than the ionospheric Debye length, it can be expected that the main part of the ion population is born in the quasi-neutral region with a potential φ_0, or where the potential is close to this value. Neglecting the small term with the negative power in $\sinh(2vv_s)$ of equation (4), the ion distribution can be written as

$$f(r,v) = \frac{C}{u}\exp\left(-(u-v_s)^2\right), \quad u = \sqrt{v^2+\Delta\chi}, \quad \Delta\chi = \frac{e}{kT}(\varphi(r)-\varphi_0). \quad (5)$$

[21] The constant C of this steady state distribution can be found from the balance between ion production inside the grid sphere and ion flux through the grid sphere surface. Assuming that the potential drop inside the grid sphere is small compared to the grid sphere surface potential accelerating the electrons, and that the approximately neutral region is large, the radial dependence of the electron flux density, j, can be neglected. So the balance between ion production and loss through the grid sphere surface can be written

$$\frac{4}{3}\pi R^3 \alpha\sigma N_a j = 4\pi R^2 v_T^4 \int f(R,v) v_n dv^3, \quad (6)$$

where v_n is the ion velocity component normal to the grid sphere surface. The calculation of ion flux density on the right-hand side of the expression (6) is presented in Appendix A, (A1) and (A2). The normalization constant, C, in the ion distribution (5) can be expressed using equation (6) and the result is

$$C = \frac{2\alpha R j \sigma N_o}{3\pi v_T^4 \Gamma(v_s,\Delta\chi_R)}, \quad \Delta\chi_R = \frac{e}{kT}(\varphi_R - \varphi_0), \quad (7)$$

where φ_R is the potential of the grid sphere surface, φ_0 is the potential at the point where the ion is produced, and $\Gamma(v_s, \Delta\chi_R)$ is defined by equation (A2).

[22] So the ion density can be found by integration of the distribution function (5), and (7) over the velocity $\vec{v}$. The domain of integration in velocity space is restricted by the condition that the ion kinetic energy should be smaller then the depth of the potential well. The ion density calculations are presented in Appendix A. It is found (A5) that

$$n(r) = 2\left(\sqrt{\pi}v_T\right)^3 C[\Psi(v_s,\Delta\chi) - \Psi(v_s,\Delta\chi_R)], \quad (8)$$

with the coefficient C defined by equation (7).

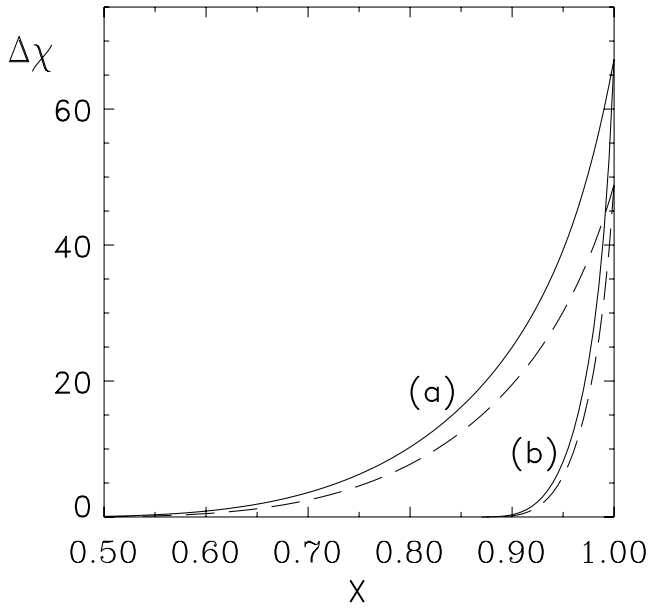

Figure 5. Normalized potential distribution inside the grid sphere, $\Delta\chi = e(\varphi(r) - \varphi_0)/kT$. Cases a and b correspond to parameters $\Pi_1 = 9 \times 10^5$ and $\Pi_1 = 1.5 \times 10^7$, respectively. For the solid lines, $\Pi_2 = 0.002$, and for the dashed lines, $\Pi_2 = 0.0243$.

[23] To calculate the density of the penetrating electrons we assume a one-dimensional acceleration inside the grid sphere. This assumption has been used by *Laframboise* [1997] in the model of current collection for the region just outside the solid surface and in our model for current collection presented in section 2. As shown above, the results from this model are in reasonable agreement with the experimental data from the TSS 1 and TSS 1R missions. We expect that the potential drop inside the grid sphere is small compared to the grid sphere surface potential. If the electric field near the surface inside the grid sphere is comparable to the electric field outside it, the character of the density distribution will also remain close to the character of the density distribution outside the grid sphere surface. It is in this inner region near the grid sphere surface that the main part of the total inner potential drop, $\Delta\chi_R$, takes place. Deeper inside, and farther from the surface, the change of potential is small and therefore the same will be true for the density, taking into account that the potential drop, $\Delta\chi_R$, is small compared to the electron energy. Then the electron density into the sphere can be written

$$n_e = \alpha j \sqrt{\frac{m}{2e\varphi(r)}}, \tag{9}$$

where the potential can be expressed using $\Delta\chi$ and $\Delta\chi_R$ from equations (5) and (7) ($e\varphi(r) = e\varphi_R + kT(\Delta\chi - \Delta\chi_R)$). Equating the ion density (8) to the electron density (9), and setting $\Delta\chi$ equal to zero, the quasi-neutrality condition can be written

$$\frac{4\sqrt{\pi}}{3}\sigma N_0 R\sqrt{\frac{M}{m}\left(\frac{e\varphi_R}{kT} - \Delta\chi_R\right)} = \frac{\Gamma(v_s, \Delta\chi_R)}{\Psi(v_s, \Delta\chi = 0) - \Psi(v_s, \Delta\chi_R)}, \tag{10}$$

where the values of Γ and Ψ are defined by equations (A2) and (A5) respectively. As can be seen from this equation, the depth of the potential well, $\Delta\chi_R$, for fixed values of electron temperature and neutral particle density, depends only on the satellite velocity and the grid sphere potential, but not on the grid sphere transparency. The left-hand side of equation (10) is the product of two terms: the ratio of the grid sphere size to the electron free path between ionization collisions; and a term primarily dependent on the grid sphere potential. It was found that the well depth, $\Delta\chi_R$, is inversely proportional to the magnitude of these dimensionless parameters, so that for larger parameters the depth is smaller. This depth is of the same order of magnitude as the kinetic energy of the oxygen ion motion relative to the satellite (~5 eV). For the combination of $\sigma N_o R = 6 \times 10^{-5}$ and grid sphere potentials 100 V and 1000 V, the well depth is 5.7 V and 4.9 V, respectively, while for $\sigma N_o R = 5 \times 10^{-6}$ the potential drops are 7.2 V and 6.6 V. If the parameter $\sigma N_o R$ changes from 6×10^{-5} to 5×10^{-6}, for a grid sphere potential of 500 V, the well depth changes from 5.2 V to 6.8 V.

[24] These magnitudes for the potential well are calculated using equation (8) for the ion density obtained with the help of the mathematical approximation (A5) discussed in Appendix A. While these results are needed for the self-consistent calculation of the potential distribution inside the grid sphere presented below, the depth of the potential well can also be calculated using the exact ion density (A4) from Appendix A. The difference in the depth of the potential well from both calculations is less then 10%, that is, the same order as the accuracy of the mathematical approximation used in the ion density calculations, as discussed in Appendix A.

[25] We assumed above that in most of the grid sphere interior, the potential is close to the potential determined by neutrality, and the electric field near the grid sphere surface is large. If either assumption does not hold, the expressions for the ion and electron densities are not valid. To check these assumptions and to calculate the potential distribution, $\Delta\chi$, inside the grid sphere the Poisson equation should be solved. With the densities defined by equations (7)–(9) this equation can be presented as

$$\frac{1}{x^2}\frac{d}{dx}x^2\frac{d\Delta\chi}{dx} = \Pi_1\left(\frac{1}{\sqrt{\chi_R + \Delta\chi - \Delta\chi_R}} - \Pi_2\frac{\Psi(v_s, \Delta\chi) - \Psi(v_s, \Delta\chi_R)}{\Gamma(v_s, \Delta\chi_R)}\right), \tag{11}$$

$$\Pi_1 = \frac{R^2}{\lambda_D^2}\frac{\alpha j}{n_\infty v_T}\sqrt{\frac{m}{M}}, \quad \Pi_2 = \frac{4\sqrt{\pi}}{3}\sqrt{\frac{M}{m}}\sigma N_0 R, \quad x = \frac{r}{R},$$

where the first term on the right-hand side is the electron density and $x(= r/R)$ is the radial coordinate r normalized to the grid sphere radius R. Fixing both the potential well depth, $\Delta\chi_R$, calculated from the quasi-neutrality condition, and the potential on the grid sphere surface χ_R, we vary the derivative at the grid sphere surface until at some point inside the grid sphere both the potential and its

derivative become zero. Equation (11) has been solved for the grid sphere potentials 100 V, 500 V, and 1000 V for $\Pi_1 = 9 \times 10^5$, 1.5×10^7; and $\Pi_2 = 0.002$, 0.0243, which for a grid sphere with radius 10 m are approximately the maximum and minimum values of Π_1, Π_2 at altitudes of 300–500 km and thermal energy 0.1 eV. We chose a flux density j roughly equal to the Parker-Murphy limit. Figure 5 plots the solution of equation (11) for the grid sphere potential 500 V and Π_1, Π_2 parameters listed above. As can be seen from Figure 5, the potential distribution strongly depends only on parameter Π_1, and in particular, on the electron Debye length. For denser plasma, that is, for larger parameter Π_1, the region where the potential is close to quasi-neutral is also larger. The dependence on parameter Π_2 and therefore on the oxygen neutral density is slight. The same dependence on the parameters Π_1, Π_2 holds for the grid sphere surface potentials of 100 V and 1000 V. Figure 6 plots the dependence of the potential distribution on the grid sphere surface potential, holding parameters Π_1, Π_2 fixed. As can be seen from Figures 5 and 6, even in the case where the potential changes more gradually, most of the grid sphere interior has a potential close to neutrality. This validates the assumption above that ions are born mostly in the region where the potential is close to the potential of a quasi-neutral plasma. The extent of this region depends primarily on the parameter Π_1, and therefore on the plasma density. For the system parameters considered above, the density is high enough to create such a region. In this sense the plasma is dense, as has been initially assumed. The potential distribution presented by Figures 5 and 6 is also consistent with the assumption that the potential drops near the grid sphere surface and that the electric field in this region is strong, supporting the choice of the electron density distribution.

[26] We calculated the depth of the potential well for system parameters such that the main ion population is produced in the region where the potential is close to quasi-neutral. This simplifies the calculation of the ion density, because the potential $\varphi(r_0)$ in distributions (3)–(5) is constant for all particles, but if this region is small this simplification fails. Because the depth of the potential well is defined by the balance between ion production and loss through the grid sphere surface, smaller production rates deepen the potential well and shrink the quasi-neutral region. This can be seen in Figure 5, where smaller production rates correspond to smaller parameter Π_2 in equation (11). As can be seen from distribution (5) for the satellite velocity $v_s = 7.31$, a well depth of about 10 V will confine practically all produced ions so reducing the ion production rate only shrinks the quasi-neutral region. Therefore as long as a quasi-neutral region exists inside the grid sphere, the depth of the potential well will be about the same order of magnitude as found in the calculations above.

[27] While a solid sphere contactor collects current only in the ram hemisphere, a grid sphere collects current in both. Since the potential well inside the grid sphere is small compared to the energy of the electrons accelerated by the grid sphere surface potential, the electrons should be able to cross and leave the grid sphere interior through the wake hemisphere if they do not intersect the mesh. These electrons will be attracted back by the grid sphere potential, and may add to the collected current.

4. Region Outside the Grid Sphere and Grid Sphere Current Collection

[28] We now use the model developed above to estimate an upper bound for the current collected by the grid sphere. First we return to the assumptions of solid sphere current collection presented in section 2 and discuss to what degree they are applicable to a grid sphere. We assumed that a positively charged sphere should reflect the incoming ions, so that the potential of the reflecting region is determined by the satellite orbital velocity. Clearly this potential should be independent of the sphere transparency and as valid for the grid sphere as for the solid one. We did not consider the structure of this region, but assumed that the boundary of this region collects the upper limit current in magnetized plasma, calculated according to *Laframboise and Parker* [1973]. This is still consistent with our goal of estimating the maximum collectable current. Neglecting the structure of the region where the incoming ions are reflected, we also assumed elastic reflection, and that the ion density at the inner boundary is twice the undisturbed ion density. Further, we assumed that the electron density at this boundary equals the ion density, because of the supposition that the plasma is close to neutral. These assumptions hold also for the grid sphere, but now the electron density at the boundary will include a contribution from the flux passing through the grid sphere. It is less clear how the grid sphere transparency will affect the electron density distribution that has been assumed for the region between the ion reflecting boundary and the sphere surface in equation (2) and therefore the radius of the current collecting boundary in equation (1). We do not think that the electron distribution will change drastically, however, for the following reasons.

[29] As can be seen from Figures 3 and 4, the results from the Alpert model are close to the experimental data, where the model assumes a solid sphere at rest in plasma without a magnetic field. Alternatively it is known [*Alpert et al.*, 1965] that under the same conditions, the potential distribution around a charged sphere is strongly affected by particle reflection from the body surface only if the reflection is very close to perfect, $1 - q \ll R/l$, where q is the reflection coefficient and l is the particle free path. For the grid sphere there also exists a flux from the sphere surface that could be considered, at least qualitatively, as the flux of reflected particles with a "reflection coefficient" roughly equivalent to the grid sphere transparency. Since the inequality above is not satisfied, we expect that the character of the potential distribution given by the Alpert model will not change dramatically if applied to a grid sphere. Because the results of our calculations and the results of the Alpert model agree with the data for a variety of plasma densities and potentials where the condition $e\varphi_R/kT \geq (R/\lambda_D)^{4/3}$ holds, we expect that our choice of the electron density distribution, verified for a solid sphere, is also valid for a grid sphere. Therefore, to estimate the maximum current collected by a grid sphere, we calculate the current collected by a solid sphere for the same system parameters, and assume that the current collected by a grid sphere is equal to this current times

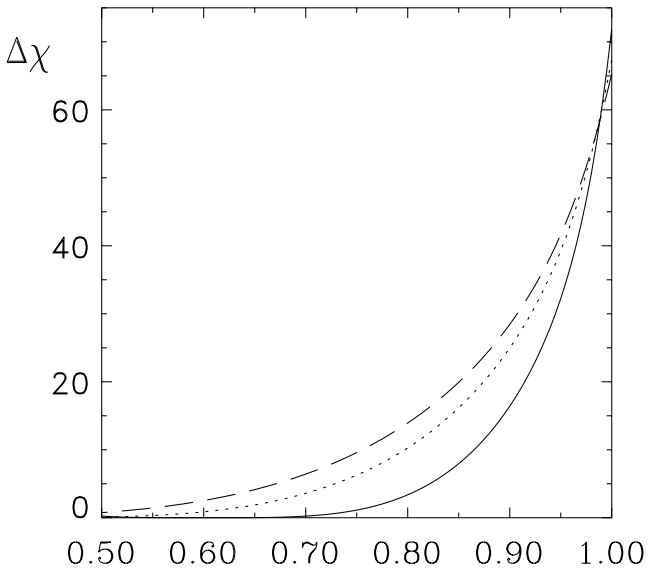

Figure 6. Normalized potential distribution inside the grid sphere, $\Delta\chi = e(\varphi(r) - \varphi_0)/kT$, with $\Pi_1 = 9 \times 10^5$ and $\Pi_2 = 0.002$ for different grid sphere surface potentials: $e\varphi_R/kT = 10^3$ (solid line), $e\varphi_R/kT = 5 \times 10^3$ (dotted line), and $e\varphi_R/kT = 10^4$ (dashed line).

the opacity, the probability the electron collides with the mesh before leaving the interaction region. According to section 3, electrons are one-dimensionally accelerated by the grid sphere surface potential, but their density is approximately isotropic inside the grid sphere. The electron penetrates inside the grid sphere with a probability equal to the grid sphere transparency α. We assume that this electron can reach either the ram or the wake hemisphere from inside the grid sphere with equal probability, 1/2. If the electron intersects the ram hemisphere it can escape the region of interaction with a total probability equal to the product of the probability to enter the grid sphere, α, the probability to reach the ram hemisphere, 1/2, and the probability to exit through the mesh, α, that is, with total probability $\alpha^2/2$. This is also the probability that the electron will be found in the wake hemisphere. To estimate an upper limit for the collected current, we assume that if the electron after the first passage exits in the wake region alone it is attracted back by the grid sphere, intersecting the grid sphere surface two more times before finally leaving the interaction region. The probability that the electron will return from the wake region inside the grid sphere is the product of the probability to reach the wake region, $\alpha^2/2$, calculated above, and the probability to avoid the mesh twice, α^2, that is, $\alpha^4/2$. As the result, an electron is able to intersect the region of interaction and escape into the surrounding plasma with the probability $\alpha^2/2 + \alpha^4/2$. So, for this scenario the collected current is

$$I_{gs} \approx \left(1 - \frac{\alpha^2}{2} - \frac{\alpha^4}{2}\right) I_{ss}. \tag{12}$$

Here I_{gs} is the current collected by the grid sphere, and I_{ss} is the current collected by the solid sphere. The normalized current I_{ss}/I_0 for a solid sphere with radius 10 nm for typical plasma densities and particle thermal energy 0.1 eV is presented in Table 4 in the two first rows. With the help of this ratio and equation (12) for the grid sphere for a given transparency and potential, the collected current can be estimated. In Table 4 this current is presented in the two last rows in amperes where the transparency is taken to be 90%.

5. Discussion and Conclusions

[30] In this paper we have estimated the maximum current that can be collected by a grid sphere. This calculation takes into account the orbital grid sphere motion and ion production inside the grid sphere due to impact ionization by incoming electrons accelerated by the grid sphere surface potential. These two processes lead to the formation of a small potential well inside the grid sphere. For grid sphere potentials of 100 V and 1000 nV, the well depth has been found to be in the range of 5 V to 7 V, respectively. So the depth of this potential well is comparable to the energy of the ions born inside the sphere, which is defined by the relative velocity between the neutrals and the satellite. Such a small potential drop means that the electron motion inside the grid sphere will be only slightly affected by this electric field. Electrons will crossover the grid sphere interior and some fraction of uncollected electrons penetrating the ram hemisphere will leave the grid sphere through the wake hemisphere. These electrons will be attracted back by the grid sphere potential and will additionally intersect the grid sphere surface. So the effective opacity of the grid sphere will be higher than that defined by the mesh transparency and a larger current can be collected.

[31] We base this estimate of the grid sphere current collection on the proposed model of the current collection by a solid sphere contactor. Results of the TSS 1 and TSS 1R sphere contactors demonstrated that the collected currents differ significantly from that predicted by the Parker-Murphy model [*Parker and Murphy*, 1967] as can be seen in Figures 3 and 4. So this model has been modified by different authors taking into account the satellite motion, ion reflection, and higher electron temperatures observed in the experiment. The results obtained by *Dobrowolny et al.* [1995] (Figure 3) and *Laframboise* [1997] with these modifications are in a good agreement with the observations of the TSS 1 mission. The curve in Figure 10 of *Laframboise* [1997] is very close to the carve P-M 2 in Figure 3. When *Laframboise* [1997] compared his model with the preliminary results from the TSS 1R flight, he concluded that the model needed further modification. Good agreement with TSS 1R data has been found by *Cooke and Katz* [1998], but they did not discuss the currents collected by the TSS 1 mission. Data from both flights have also been compared with the prediction for the collected currents from the Alpert model [*Alpert et al.*, 1965] for unmagnetized plasma and contactor at rest by *Dobrowolny et al.* [1995] and *Vannaroni et al.* [1998]; which agree with the measurements (Figures 3 and 4) only if the inequality $e\varphi_R/kT \geq (R/\lambda_D)^{4/3}$ is valid.

[32] The main components of our model (reflection of incoming ions, potential and density distribution in this

Table 4. Normalized Current I_{ss}/I_0 Collected by the Solid Sphere (First Two Rows) and Current Collected by the Grid Sphere I_{gs} (A) With the Same Radius, 10 m (Last Two Rows)

	φ_R, V		
n_∞ 10^{-10}, m^{-3}	100	500	1000
5	2.9	4.1	5.3
70	2.5	2.8	3.1
5	0.4	0.6	0.7
70	5.1	5.7	6.4

reflecting region, one-dimensional electron acceleration near the sphere surface, upper limit for current collection in the magnetic field) have been discussed in a number of studies, in particular related to the TSS 1 and TSS 1R missions [*Laframboise and Parker*, 1973; *Laframboise and Sonmor*, 1993; *Dobrowolny et al.*, 1995; *Vannaroni et al.*, 1998; *Katz et al.*, 1994; *Laframboise*, 1997; *Cooke and Katz*, 1998; *Ma and Schunk*, 1998; *Singh and Leung*, 1998]. The modification we propose is based on the assumption that the current collecting region can be divided in two parts: an outer region collecting the upper limit current permitted for two-dimensional electron acceleration, and an inner region where the electron density distribution is determined by one-dimensional acceleration. The boundary between these two regions is approximately defined as the point where the electric field abruptly changes. This is the element that has not been used in previous models. The approach appears to be reasonable, and the currents calculated from our model are in good agreement with the currents measured by the TSS 1 and TSS 1R missions. So, it can be hypothesized that this boundary between the two regions of disturbed plasma near a solid body, as introduced in the model, is a robust characteristic of the process of current collection, at least for high enough (>20V) sphere potentials.

[33] We can use this estimate of the maximum current collected by a grid sphere to compare the advantage of such an anode design for mass and drag reduction. The drag force, caused by collisions with neutrals, is proportional to the grid sphere surface solid fraction multiplied by two, because of the interaction with the outer surface of the ram hemisphere and the inner surface of the wake hemisphere. So

$$F_{gs} = 2(1-\alpha)F_{ss}, \tag{13}$$

where F_{gs} and F_{ss} are the friction forces acting on the grid sphere and the solid sphere respectively. From equations (12) and (13) it follows that the drag per unit of collected current for a grid sphere with a transparency of 80–95% is approximately 1.2–1.4 times smaller than for a solid sphere with the same radius, while the reduction in the mass per unit current is 2.4–2.8 times. We can also compare these two anode designs at a fixed current. Since the current collected by a solid sphere depends on the sphere radius as $I_{ss} \propto R^2/R^{2\sigma}$, where σ is defined only by the sphere potential (section 2), equating the currents (equation (12)) gives their radii as

$$\frac{R_{gs}}{R_{ss}} = \left(1 - \frac{\alpha^2}{2} - \frac{\alpha^4}{2}\right)^{\frac{1}{2(\sigma-1)}}. \tag{14}$$

The mass and drag ratios for these anodes are

$$\frac{M_{gs}}{M_{ss}} = \left(\frac{R_{gs}}{R_{ss}}\right)^2 (1-\alpha), \quad \frac{F_{gs}}{F_{ss}} = 2\frac{M_{gs}}{M_{ss}}, \tag{15}$$

and for the range of parameters presented in Table 4 these ratios have a well expressed minimum as a function of the grid sphere transparency α. For normalized grid sphere potentials in the range $e\varphi_R/kT = 10^3$–10^4 this minimum corresponds to the range of transparencies $\alpha = 0.9$–0.76, with corresponding mass ratios $M_{gs}/M_{ss} = 0.45$–0.56, and a drag ratio of about one. Of course the anode designs should be compared taking into account specific mission requirements, such as the needed current.

Appendix A: Ion Density Inside the Grid Sphere

[34] 1. The normalization constant, C, in the ion distribution function (5) has been calculated from equation (6). The ion flux density through the grid sphere surface on the right-hand side of this equation in spherical coordinates in velocity space is

$$\begin{aligned} I &= \int f(R,v) v_n dv^3 \\ &= C \int_0^{2\pi} d\phi \int_0^{\pi/2} \sin\vartheta d\vartheta \int_0^{\infty} \frac{v\cos\vartheta}{u} e^{-(u-v_s)^2} v^2 dv, \end{aligned} \tag{A1}$$

where $u(R) = \sqrt{v^2 + \Delta\chi_R}$, and $\Delta\chi_R = e(\varphi_R - \varphi_0)/kT$ is the normalized potential drop between the grid sphere surface (φ_R) and the neutral region (φ_0). The result of the integration (with the change from the variable v to the new variable $u(R)$) is

$$\begin{aligned} I &= \frac{\pi}{2} C\Gamma, \Gamma \\ &= z_+^R \exp\left(-\left(z_-^R\right)^2\right) + \sqrt{\pi}\left(z_+^R z_-^R + \frac{1}{2}\right)\left(1 + \frac{z_-^R}{|z_-^R|} erf\left(|z_-^R|\right)\right), \end{aligned} \tag{A2}$$

where $z_\pm^R = v_s \pm \sqrt{\Delta\chi_R}$. The normalization constant C (5) then can be found with the help of this expression for I substituted in equation (6).

[35] 2. The ion density for the distribution function (5), (7) can be found as

$$n(r) = 4\pi v_T^3 C \int_0^{\sqrt{\Delta\chi_R - \Delta\chi}} \frac{v^2}{u} e^{-(u-v_s)^2} dv, \tag{A3}$$

where $u(r) = \sqrt{v^2 + \Delta\chi}$ and $\Delta\chi = e(\varphi(r) - \varphi_0)/kT$. The ions able to reach the grid sphere surface with nonzero velocity are lost, and their contribution to the density is negligible in equilibrium because of their small production rate and transit time, as has been found in section 3. Under these conditions the upper limit of the integral follows from

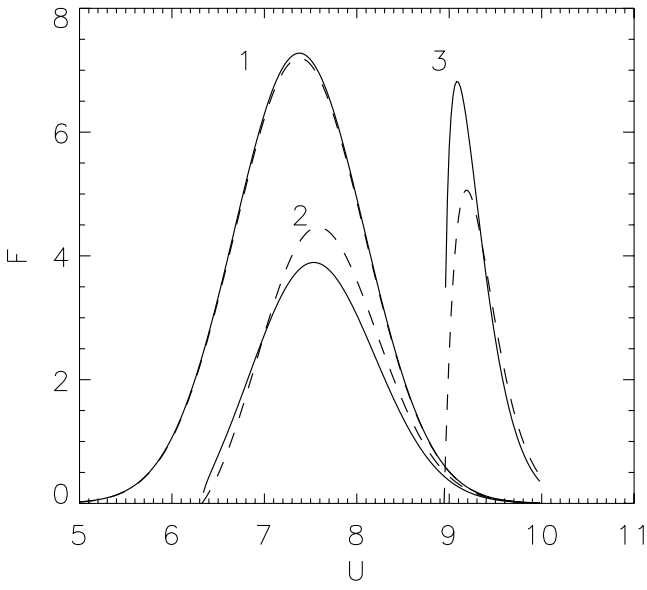

Figure A1. Comparison of the exact (solid lines) and approximate (dashed lines) integrands F for the ion density calculations for parameters $\Delta\chi = 1$ (curve 1), $\Delta\chi = 40$ (curve 2), and $\Delta\chi = 80$ (curve 3). For $\Delta\chi = 80$, the integrands are enlarged a hundred times.

energy conservation, $MV^2/2 + e\varphi(r) = MV_R^2/2 + e\varphi_R$. For $\Delta\chi = 0$ the result of the integration is

$$n(r_0) = 2\left(\sqrt{\pi}v_T\right)^3 C\left(\sqrt{\pi}\left(e^{-v_s^2} - e^{-\left(\sqrt{\Delta\chi_R}-v_s\right)^2}\right) + v_s\left(1 - \mathrm{sgn}\left(v_s - \sqrt{\Delta\chi_R}\right)erf\left(\left|v_s - \sqrt{\Delta\chi_R}\right|\right)\right)\right). \quad \text{(A4)}$$

[36] An approximate expression for the integrand in the equation (A3) has been used to obtain an analytic expression for the density, if $\Delta\chi$ is comparable to $\Delta\chi_R$. After a change of variable v to $u(r) = \sqrt{v^2 + \Delta\chi}$, the integrand $F = \sqrt{u^2 - \Delta\chi}\exp(-(u - v_s)^2)$ has been approximated by the function $(u - \sqrt{\Delta\chi}/v_s)(1 - \exp(\sqrt{\Delta\chi} - u))\exp(-(u - v_s)^2)$, where the satellite velocity, normalized to the velocity of the oxygen ions that weakly changes in the altitude range 300–500 km, has been taken to be $v_s = 7.31$. The potential well depth that has been found with the help of the equation (A4) in section 3, for system parameters considered in this paper is restricted by condition $\Delta\chi_R < 75$. Both integrands are plotted in Figure A1 for different magnitudes of $\Delta\chi$. As can be seen from Figure A1, the error of such approximation results in a difference in the areas not larger than 10%. With this approximation the ion density is

$$n(r) = 2\left(\sqrt{\pi}v_T\right)^3 C(\Psi(v_s, \Delta\chi) - \Psi(v_s, \Delta\chi_R)) \quad \text{(A5)}$$

$$\Psi(v_s, \Delta\chi) = \left(v_s - \frac{\sqrt{\Delta\chi}}{v_s}\right)(1 + \mathrm{sgn}(z_-)erf(|z_-|)) - \left(v_s - \frac{\sqrt{\Delta\chi}}{v_s} - \frac{1}{2}\right)(1 + \mathrm{sgn}(z_- - 0.5) \cdot erf(|z_- - 0.5|))e^{-z_- + \frac{1}{4}}$$

$z_- = v_s - \sqrt{\Delta\chi}$

$\Psi(v_s, \Delta\chi_R)$ is the function $\Psi(v_s, \Delta\chi)$ calculated for $\Delta\chi = \Delta\chi_R$.

[37] **Acknowledgments.** The work described in this paper was funded in part by the In-Space Propulsion Technology Program, which is managed by NASA's Science Mission Directorate in Washington, D.C., and implemented by the In-Space Propulsion Technology Office at the Marshall Space Flight Center in Huntsville, Alabama, under Technical Task Agreement M-ISP-04-37. The program objective is to develop in-space propulsion technologies that can enable or benefit near-term and midterm NASA space science missions by significantly reducing cost, mass, or travel times. Emmanuel Krivorutsky, who held an NRC position when this work has been performed, is grateful to L. Avanov for help with the computing.

[38] Arthur Richmond thanks David N. Walker and another reviewer for their assistance in evaluating this paper.

References

Alpert, Y. L., A. V. Gurevich, and L. P. Pitaevskii (1965), Disturbance of the plasma and the electric field in the vicinity of a charged body at rest, in *Space Physics and Artificial Satellites*, p. 186, Consult. Bur., New York.

Cooke, D. L., and I. Katz (1998), TSS-1R electron currents: Magnetic limited collection from a heated presheath, *Geophys. Res. Lett.*, *25*, 753.

Dobrowolny, M., U. Guidoni, E. Melchioni, G. Vannaroni, and J. P. Lebreton (1995), Current-voltage characteristics of the TSS 1 satellite, *J. Geophys. Res.*, *100*, 23,953.

Katz, I., E. Melchioni, M. Mandell, M. Oberhardt, D. Thompson, T. Neubert, B. Gilchrist, and C. Bonifazi (1994), Observations of ionosphere heating in the TSS-1 subsatellite presheath, *J. Geophys. Res.*, *99*, 8961.

Laframboise, J. G. (1997), Current collection by a positively charged spacecraft: Effects of its magnetic presheath, *J. Geophys. Res.*, *102*, 2417.

Laframboise, J. G., and L. W. Parker (1973), Probe design for orbit-limited current collection, *Phys. Fluids*, *16*, 629.

Laframboise, J. G., and L. J. Sonmor (1993), Current collection by probes and electrodes in space magnetoplasmas: A review, *J. Geophys. Res.*, *98*, 337.

Ma, T. Z., and R. W. Schunk (1998), 3-D time-dependent simulations of the tethered satellite-ionosphere interaction, *Geophys. Res. Lett.*, *25*, 737.

Parker, L. W., and B. L. Murphy (1967), Potential buildup on an electron-emitting ionospheric satellite, *J. Geophys. Res.*, *72*, 1631.

Schunk, R. W., and A. F. Nagy (2000), *Ionospheres: Physics, Plasma Physics, and Chemistry*, Cambridge Univ. Press, New York.

Singh, N., and W. C. Leung (1998), Numerical simulation of plasma processes occurring in the ram region of the tethered satellite, *Geophys. Res. Lett.*, *25*, 741.

Stone, N. H., and P. A. Gierow (2001), A preliminary assessment of passive end-body plasma contactors, paper presented at 39th Aerospace Sciences Meeting, Am. Inst. of Aeronaut. and Astronaut., Reno, Nev., 8–11 Jan.

Stone, N. H., J. D. Moore, W. R. Clayton, and P. A. Gierow (2002), A preliminary assessment of grid-spheres used as end-body electrodes for electrodynamic tethers, CP608, *Space Technology and Applications International Forum—STAIF 2002*, edited by M. S. El-Genk, p. 537, Am. Inst. of Phys., Albuquerque, N. M.

Thompson, D. C., C. Bonifazi, B. Gilchrist, S. D. Williams, W. J. Raitt, J. P. Lebreton, W. J. Burke, N. H. Stone, and K. H. Wright Jr. (1998), The current-voltage characteristics of a large probe in low Earth orbit: TSS-1R results, *Geophys. Res. Lett.*, *25*, 413.

Vannaroni, G., M. Dobrowolny, J. P. Lebreton, E. Melchioni, F. De Venuto, C. C. Harvey, L. Less, U. Guidoni, C. Bonifazi, and F. Mariani (1998), Current-voltage characteristic of the TSS-R satellite: Comparison with isotropic and anisotropic models, *Geophys. Res. Lett.*, *25*, 749.

Wright, K. H., N. H. Stone, J. D. Winningham, D. Curgiolo, C. Bonifazi, B. Gilchrist, M. Dobrowolny, F. Mariani, and D. Hardy (1996), Satellite particle collection during active states of the tethered satellite system (TSS), *AIAA Pap. 96-2298*, Am. Inst. of Aeronaut. and Astronaut., New York.

G. V. Khazanov, E. Krivorutsky, and R. B. Sheldon, National Space Science and Technology Center, NASA Marshall Space Flight Center, Huntsville, AL 35805, USA. (george.khazanov@msfc.nasa.gov)